Intraseasonal SST Variability and Air–Sea Interaction over the Kuroshio Extension Region during Boreal Summer*

LU WANG

LASG, Institute of Atmospheric Physics, Chinese Academy of Sciences, and Graduate University of Chinese Academy of Sciences, Beijing, China

TIM LI

IPRC, and Department of Meteorology, University of Hawaii at Manoa, Honolulu, Hawaii

TIANJUN ZHOU

LASG, Institute of Atmospheric Physics, Chinese Academy of Sciences, Beijing, China

(Manuscript received 20 February 2011, in final form 23 August 2011)

ABSTRACT

The structure and evolution characteristics of intraseasonal (20–100 day) variations of sea surface temperature (SST) and associated atmospheric and oceanic circulations over the Kuroshio Extension (KE) region during boreal summer are investigated, using satellite-based daily SST, observed precipitation data, and reanalysis data. The intraseasonal SST warming in the KE region is associated with an anomalous anticyclone in the overlying atmosphere, reduced precipitation, and northward and downward currents in the upper ocean. The corresponding atmospheric and oceanic fields during the SST cooling phase exhibit a mirror image with an opposite sign. A mixed layer heat budget analysis shows that the intraseasonal SST warming is primarily attributed to anomalous shortwave radiation and latent heat fluxes at the surface. The anomalous sensible heat flux and oceanic advection also have contributions, but with a much smaller magnitude.

The SST warming caused by the atmospheric forcing further exerts a significant feedback to the atmosphere through triggering the atmospheric convective instability and precipitation anomalies. The so-induced heating leads to quick setup of a baroclinic response, followed by a baroclinic-to-barotropic transition. As a result, the atmospheric circulation changes from an anomalous anticyclone to an anomalous cyclone. This two-way interaction scenario suggests that the origin of the atmospheric intraseasonal oscillation over the KE region may partly arise from the local atmosphere–ocean interaction.

1. Introduction

The interaction between the extratropical ocean and its overlying atmosphere is key to understanding and predicting climate variability, because a close link between the SST and the climate anomalies in local and remote regions has been confirmed by many previous studies (e.g., Namias 1959, 1965; Hendon and Hartmann 1982; Held et al. 1989; Peng et al. 1995; Kushnir et al. 2002). For example, the occurrences of warmer-than-normal water in the North Pacific are accompanied by drought conditions over subtropical East Asia (Kawamura 1994; Park and Schubert 1997), the northwest Pacific, western Canada, the U.S. northern Great Plains, and the Midwest during boreal summer (Lau et al. 2004). SST anomalies (SSTA) in the Kuroshio Extension (KE) region in the preceding spring may influence summer rainfall in eastern China (Zhu et al. 2000; Sun et al. 2008).

The questions of how the atmosphere and ocean interact in the midlatitudes and to what extent and how fast the atmosphere (ocean) responds to the ocean (atmosphere) have stimulated many studies. On the one hand, the extratropical SSTA may be regarded as a response to

* School of Ocean and Earth Science and Technology Contribution Number 8524 and International Pacific Research Center Contribution Number 832.

Corresponding author address: Tim Li, IPRC, and Dept. of Meteorology, University of Hawaii at Manoa, 2525 Correa Rd., Honolulu, HI 96822.
E-mail: timli@hawaii.edu

DOI: 10.1175/JCLI-D-11-00109.1

© 2012 American Meteorological Society

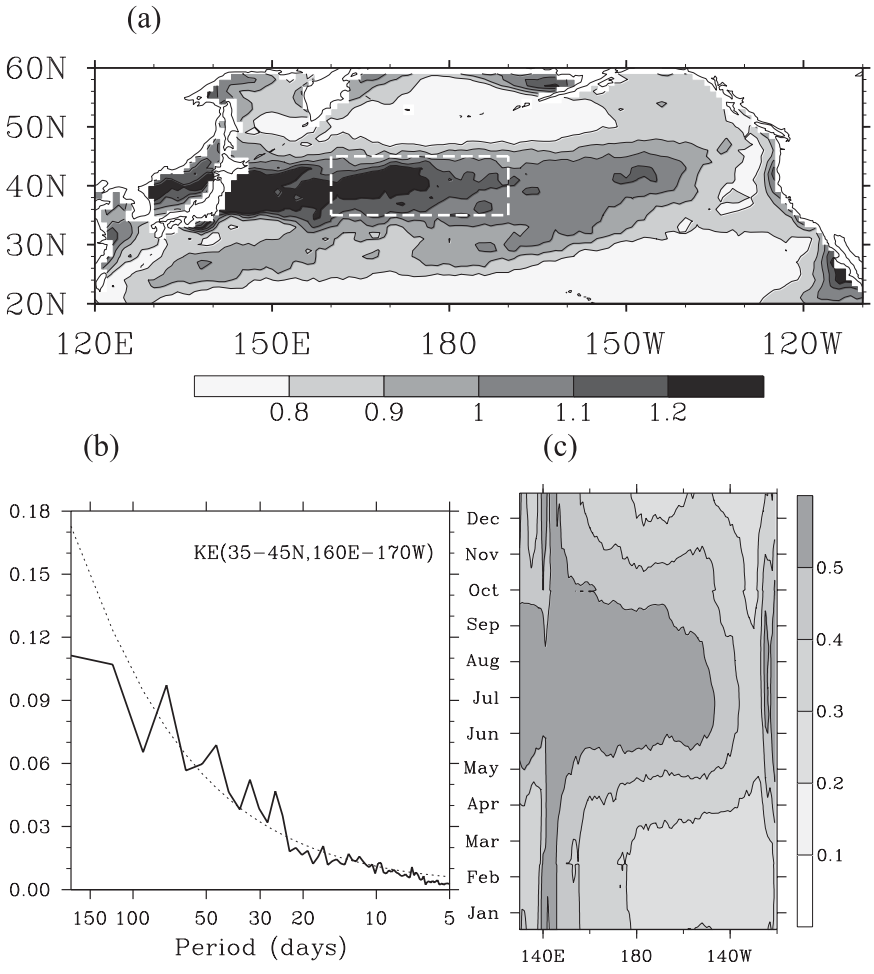

FIG. 1. (a) Standard deviation of unfiltered daily SST (K) with climatological annual cycle during 1982–2007 removed. The rectangle represents the maximum variability region over the Kuroshio Extension (KE) area (35°–45°N, 160°E–170°W). (b) Mean power spectra of the unfiltered daily SST averaged from spectra in each year over the KE region [rectangle in (a)]. The dashed line represents the 95% confidence level. (c) The amplitude of 20–100-day filtered SST along 35°–45°N throughout the year. Here the amplitude of SST on day i is calculated by the STD of the filtered SST from day ($i - 45$) to day ($i + 45$). The climatological annual cycle is obtained based on the 26-yr daily average.

fluctuations in local near-surface atmospheric conditions, such as wind speed, temperature, and humidity, that alter air–sea heat fluxes (Frankignoul and Hasselmann 1977; Frankignoul and Reynolds 1983; Frankignoul 1985; Cayan 1992; Lau and Nath 1996). The ocean dynamics such as Ekman pumping–induced upwelling and horizontal temperature advections can also contribute to SST changes (Latif and Barnett 1994; Qiu 2003), but usually with a smaller magnitude (Alexander 1992; Alexander et al. 2002; Tomita et al. 2002). On the other hand, a given midlatitude SST anomaly, in turn, can exert a significant impact on atmospheric circulation (e.g., Peng et al. 1995; Kushnir et al. 2002). Based on observational data analyses, a significant covariance was found between the 500-hPa heights during winter and the SST up to six months earlier (Czaja and Frankignoul 1999, 2002; Rodwell and Folland 2002). Numerical model experiments showed a response of an order of 10–20 gpm K^{-1} anomaly at 500 hPa in northern winter to extratropical SST anomalies with a realistic spatial pattern and amplitude.

Most previous midlatitude air–sea interaction studies focused on interannual and interdecadal time scales. In such studies, monthly mean data were often used. However, as the atmosphere evolves much faster than on a monthly time scale, some detailed characteristics of air–sea coupling may be overlooked with such a coarse dataset. The objective of the present study is to reveal the intraseasonal SST variability and associated circulation

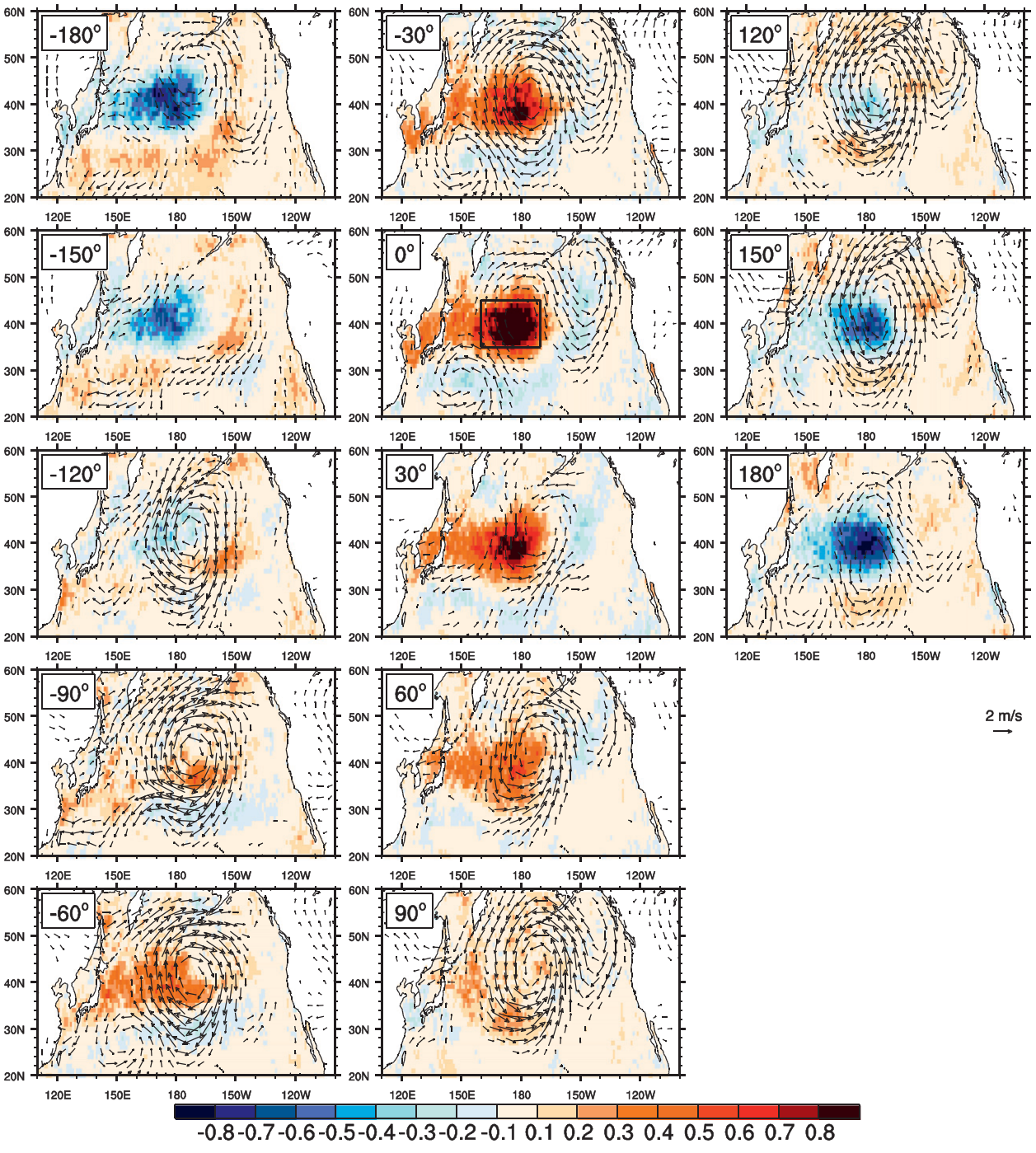

FIG. 2. Phase evolution of composite SSTA (K) (shading) and 1000-hPa wind anomalies (m s^{-1}) (vectors). The scale of the wind vector is 2 m s^{-1}. The box in phase 0° represents the region (35°–45°N, 160°E–170°W) of maximum intraseasonal SST variability.

changes in the midlatitude North Pacific [here we focused on the KE region (35°–45°N, 160°E–170°W)] that has a strong intraseasonal SST variability (shown below) using observed daily data.

Figure 1a shows the horizontal distribution of the standard deviation (STD) of unfiltered daily SST (with annual cycle removed) over the midlatitude North Pacific. A great SST variability center appears in the KE region, and the significant period (exceeding the 95% confidence level) of KE SST is within the intraseasonal (20–100 day) range (shown by the spectrum analysis in Fig. 1b). The annual cycle of amplitude of the intraseasonal SST STD

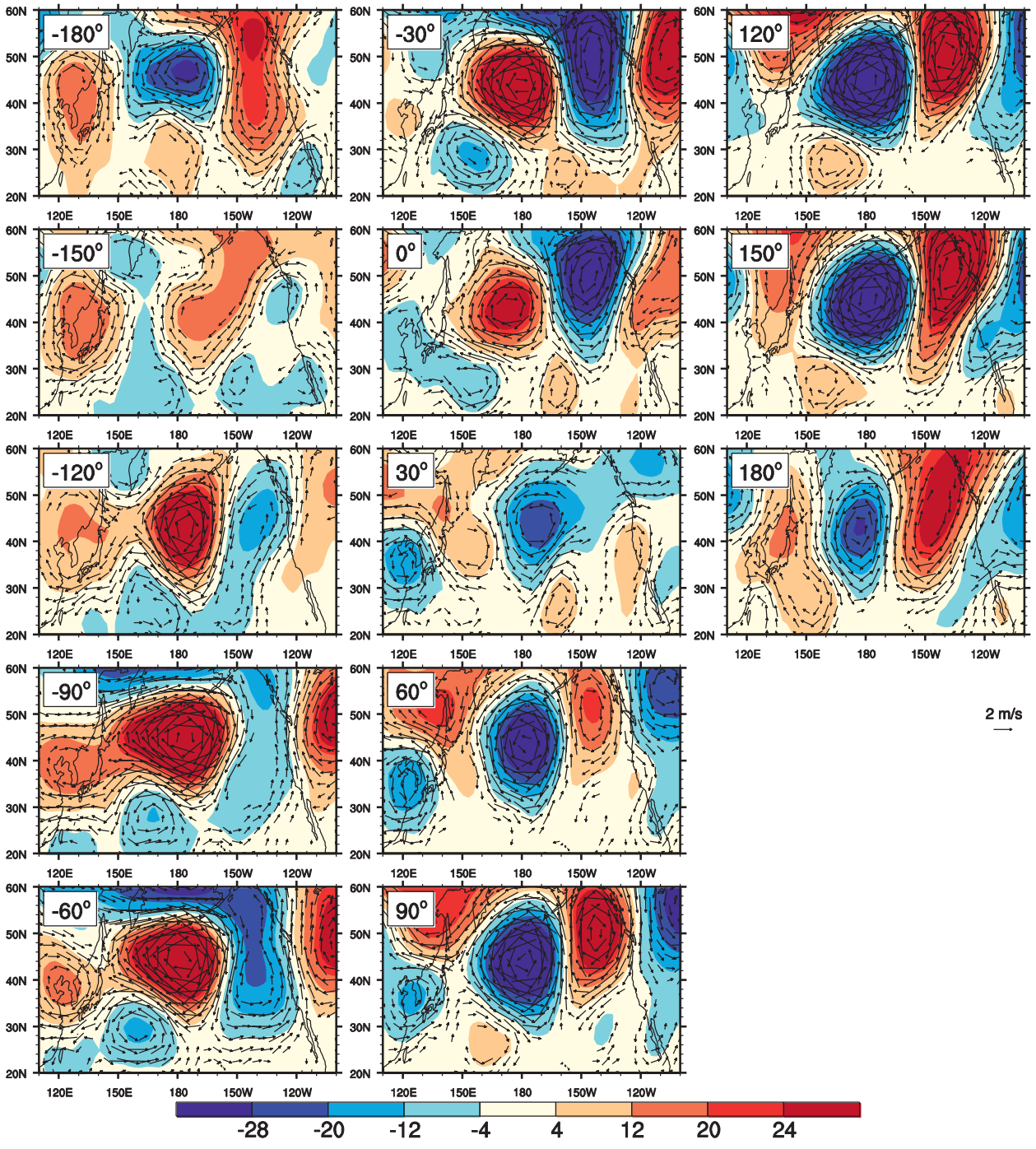

FIG. 3. Phase evolution of composite 500-hPa wind anomalies (m s^{-1}) (vectors) and 500-hPa geopotential height anomalies (gpm) (contours). The scale of the wind vector is 2 m s^{-1}.

field (Fig. 1c) shows that the intraseasonal SST variability exhibits marked seasonality, with a much stronger perturbation during boreal summer (from June to October). The magnitude of the intraseasonal SST variability in the KE region during boreal summer exceeds 0.6 K (figure not shown), which is comparable to the interannual and interdecadal counterparts. The ratio of the intraseasonal SST variability to the total SST variability (including the annual cycle and the interannual, intraseasonal, and synoptic components) is about 25% (figure not shown).

The present study is based on the observational characteristics above. The specific questions to be addressed

are the following: What causes the large intraseasonal SST variability over the KE region during boreal summer? Does the intraseasonal SSTA feed back to the overlying atmosphere and, if yes, how? The current study is separated into two parts. First, we will reveal the observed structure and evolution characteristics of the intraseasonal SST variability and associated circulation evolution feature over the KE region. Second we will investigate the mechanism responsible for the intraseasonal SST variability by conducting a mixed layer heat budget analysis, and explore the possible feedback of the intraseasonal SSTA to the atmosphere.

The remainder of the paper is organized as follows. The datasets and analysis methods are described in section 2. The observed 3D structures related to the intraseasonal SSTA are depicted in section 3. A mixed layer heat budget analysis is described in section 4 to reveal the primary contributors to the SST oscillation. The possible feedback of the SSTA to the atmosphere is examined in section 5. Finally, concluding remarks and the discussion are given in section 6.

2. Data, methods, and model

a. Data

The daily SST dataset from version 2 of the National Oceanic and Atmospheric Administration Optimal Interpolation (NOAA OI) is used in the current study. It is archived on a 0.25° × 0.25° latitude–longitude grid based upon the Advanced Very High Resolution Radiometer (AVHRR) satellite (Reynolds et al. 2002). For the atmospheric variables, the reanalysis data from the National Centers for Environmental Prediction/Department of Energy (NCEP/DOE) Reanalysis 2 (NCEP-2) (Kanamitsu et al. 2002) are employed, with a spatial resolution of 2.5° latitude × 2.5° longitude. In addition, daily outgoing longwave radiation (OLR) from NOAA (Liebmann and Smith 1996) and pentad Climate Prediction Center (CPC) Merged Analysis of Precipitation (CMAP) (Xie and Arkin 1997) data are also used.

For the mixed layer heat budget analysis, reanalysis data from the NCEP Global Ocean Data Assimilation System (GODAS) (Behringer and Xue 2004) are employed. This ocean reanalysis dataset has 1° resolution in the zonal direction and a variable grid in the meridional direction with 1/3° resolution between 10°S and 10°N. Vertically it has 40 levels with 10-m resolution in the upper 200 m. The analysis period is from 1 June to 31 October during 1982–2007, as the daily SST dataset is available from 1982. Prior to the analysis, the pentad GODAS and CMAP data are interpolated to daily values.

b. Filtering and phase composite technique

To isolate the intraseasonal signals, all variables are filtered with a Lanczos 20–100-day bandpass filter (Duchon 1979). Prior to the filtering, the climatological annual cycles are removed from raw data.

An intraseasonal SSTA index is defined as the time series of area-averaged 20–100-day filtered SST at 35°–45°N, 160°E–170°W where the maximum intraseasonal SST variance occurs (Fig. 1a). Then, a composite technique is applied to illustrate the evolution of the intraseasonal oscillation (ISO). One way is to average all selected ISO events with respect to a reference day (day 0, corresponding to each peak in the time series of a field of interest) and then plot time sequence maps at different lagged days (e.g., −30, −20, −10, 0, ...). This method may be termed as a lagged-day composite analysis. Considering the wide range of a temporal spectrum of the ISO signal over the KE region (see Fig. 1b), a large error might result when a lagged time is far from day 0. To avoid this problem, a phase composite method was adopted here. In this method, each life cycle of the oscillation is divided into 12 phases at an interval of 30°, and phase 0° represents the time when the SSTA index reaches a maximum value, that is, when the warmest intraseasonal SSTA occurs over the KE region. In contrast, phases −180° and 180° correspond to a time when the coldest intraseasonal SSTA occurs. The other phases are obtained through linear interpolation of daily data. The composite cases include only those when the SSTA index exceeds one standard deviation.

c. Budget analysis

The SST variability on the intraseasonal time scale can be diagnosed by a mixed layer heat budget analysis. Following Li et al. (2002), the temperature tendency equation is written as

$$\frac{\partial\langle T'\rangle}{\partial t} = \left(\frac{Q}{\rho C_p H}\right)' - \left\langle \overline{u}\frac{\partial T'}{\partial x}\right\rangle - \left\langle u'\frac{\partial \overline{T}}{\partial x}\right\rangle - \left\langle u'\frac{\partial T'}{\partial x}\right\rangle - \left\langle \overline{v}\frac{\partial T'}{\partial y}\right\rangle - \left\langle v'\frac{\partial \overline{T}}{\partial y}\right\rangle - \left\langle v'\frac{\partial T'}{\partial y}\right\rangle - \left\langle \overline{w}\frac{\partial T'}{\partial z}\right\rangle - \left\langle w'\frac{\partial \overline{T}}{\partial z}\right\rangle - \left\langle w'\frac{\partial T'}{\partial z}\right\rangle + R, \quad (1)$$

where Q represents the sum of net downward heat fluxes at the ocean surface, u, v, and w denote 3D ocean current velocities, R is a residual term, ρ is the density of water, C_p denotes the specific heat of water, and H represents the depth of the mixed layer that changes in space and time (in the GODAS dataset, H is defined as a depth at which

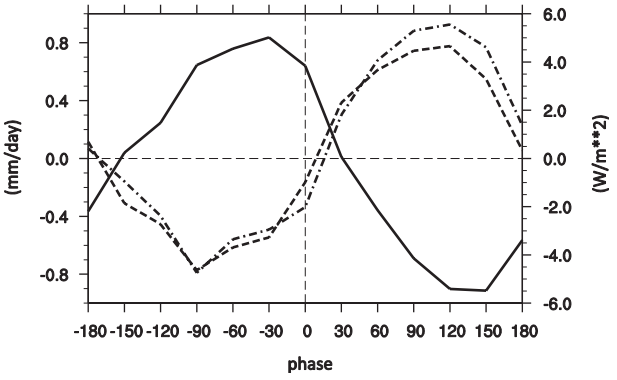

FIG. 4. Evolution of composite NOAA OLR anomalies (W m^{-2}) (solid line) and precipitation anomalies (mm day^{-1}) from CMAP (dashed line) and NCEP-2 (dashed–dotted line) averaged in the KE region (35°–45°N, 160°E–170°W).

ocean temperature is 0.8°C lower than that at surface). With the consideration of the shortwave penetration below the mixed layer, the shortwave radiation absorbed in the mixed layer can be written as (Wang and McPhaden 1999)

$$Q_{\mathrm{sw}} = Q_{\mathrm{surf}} - 0.47Q_{\mathrm{surf}}e^{-0.04H}, \qquad (2)$$

where Q_{surf} is the surface shortwave radiation and H is the mixed layer depth.

In Eq. (1), the angle brackets are defined as the vertical average from the ocean surface to the bottom of the mixed layer. A prime represents the intraseasonal (20–100 day, bandpass filtered) variable and an overbar represents the mean background variable (derived from a 100-day low-pass filter).

Similarly, the intraseasonal air temperature variation on a specific pressure level can be determined by Eq. (3) (Holton 2004):

$$\left(\frac{\partial T}{\partial t}\right)' = -\left(u\frac{\partial T}{\partial x}\right)' - \left(v\frac{\partial T}{\partial y}\right)' - \left(\omega\frac{\partial T}{\partial p}\right)' + \left(\frac{\alpha}{C_p}\omega\right)' + \left(\frac{\dot{Q}}{C_p}\right)', \qquad (3)$$

where $\dot{Q}$ is the rate of heating per unit mass due to radiation, conduction, and latent heat release, C_p denotes the specific heat of air, α denotes the specific volume of air, and u, v, ω represent the 3D velocity. The first four terms on the right-hand side are related to adiabatic processes and the last term is related to a diabatic process. The budget analysis based on Eq. (3) can give the relative importance of different processes in governing the isobaric temperature variation.

d. An anomaly AGCM

To examine the atmospheric response to a specified heating under a realistic mean state, an idealized anomaly AGCM experiment is conducted. This anomaly AGCM was constructed based on a dry version of the Princeton AGCM (Held and Suarez 1994) and has been used to examine the effect of the summer mean flow on monsoon–ENSO teleconnections (Wang et al. 2003), MJO initiation (Jiang and Li 2005), and the development of summertime synoptic wave trains in the western North Pacific (Li 2006). The model atmosphere is formulated with five evenly distributed sigma levels and a horizontal resolution of T42.

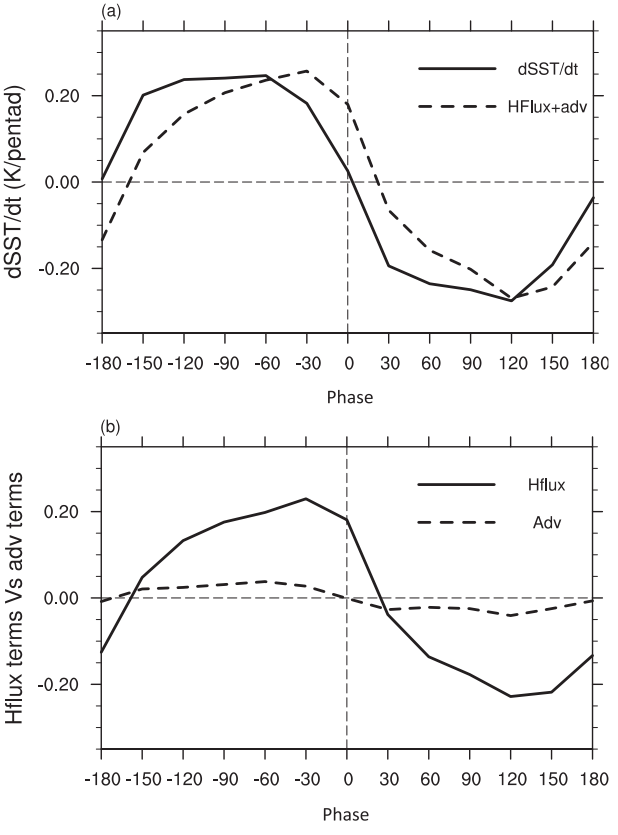

FIG. 5. (a) Evolutions of composite mixed layer temperature tendencies (K $pentad^{-1}$) (solid line) and the sum of the ocean advection and heat flux terms (K $pentad^{-1}$) (dashed line). (b) Same as (a) but for the net heat flux term (solid line) and the 3D ocean temperature advection (K $pentad^{-1}$) (dashed line).

Our strategy is to examine the local atmospheric response to a specified heating in the KE region in the presence of the 3D summer mean flow. A realistic June–October (JJASO) mean state is prescribed as the model basic state, which is taken from the long-time mean of the NCEP–NCAR reanalysis.

3. Observed characteristics of 20–100-day oscillation in North Pacific

The life cycles of the intraseasonal variability over the KE region are examined with a phase composite

technique. Figure 2 depicts the horizontal distribution of the 20–100-day filtered SSTA and corresponding wind field at 1000 hPa. To first order, the SSTAs are stationary and do not show significant movement. As defined in section 2b, the warmest SSTA over the KE region occurs at phase 0°. A large positive SSTA tendency appears from phase −150° to −30° (for simplicity, this period is defined as ''the SST developing phase''), and a negative cooling tendency appears from phase 30° to 150°. During the SST developing phase, a large-scale anomalous anticyclone appears around 40°N, 180°. The anomalous anticyclone intensifies and reaches a peak at phase −90°. Then it begins to weaken and shrink. At phases −30° and 0°, the 1000-hPa wind shows a distinct wave train pattern with an anticyclonic cell in the middle and two cyclonic cells at two sides. The wave train tilts along the southwest–northeast direction. At phase 30°, the three-cell wave train pattern disappears and an anomalous cyclonic circulation takes place in the warm SSTA region. The cyclonic circulation anomalies develop and persist in the course of the SST cooling from phase 30° to 180°.

The 500-hPa circulation anomalies in general show an in-phase evolution characteristic with those at 1000 hPa, implying an equivalent-barotropic structure (Fig. 3). A careful examination shows that the circulation centers at 500 hPa shift slightly to the north about 2°–3°. The geopotential height anomalies are consistent with the circulation anomalies (reflecting a quasigeostrophic nature), with the positive (negative) height centers corresponding to the anticyclonic (cyclonic) circulation centers.

The life cycle of 20–100-day OLR and precipitation fields over the KE region is presented in Fig. 4. The convection and rainfall anomalies are suppressed from phase −150° to −30° and are enhanced from phase 30° to 150°. The former ones are associated with the anticyclonic circulation and the latter ones are associated with the cyclonic circulation. In the following section, we will first show, through a mixed layer heat budget, how the atmospheric circulation anomalies cause the intraseasonal SSTA evolution and then demonstrate how the SSTA change further affects atmospheric convective instability/diabatic heating, which may further feed back to the transition of the atmospheric baroclinic and barotropic circulation.

4. Causes of the intraseasonal SST variation in the KE region

The observational patterns above suggest that several processes may contribute to the intraseasonal SST variation in the KE region (35°–45°N, 160°E–170°W). First, the suppressed convection (as seen in Fig. 4) associated with the anomalous anticyclone may contribute to the anomalous warming during the developing phase through enhanced downward solar radiation at the ocean surface. Second, the anomalous easterly associated with the anticyclone cell in the KE region (box as seen in Fig. 2) may oppose the summer mean westerly (figure not shown), leading to a decrease of the upward latent and sensible heat fluxes (due to reduced surface wind speed) from the ocean and thus an increase of SST. Third, the northward ocean surface currents as inferred from the surface anticyclonic cell may induce positive temperature advection and increase the SST in the region. Fourth, the downwelling upper-ocean velocity as inferred from the surface anticyclonic wind stress may suppress vertical mixing and induce a positive SSTA in situ. In addition, other processes such as longwave radiative flux and zonal oceanic advection may also play a role.

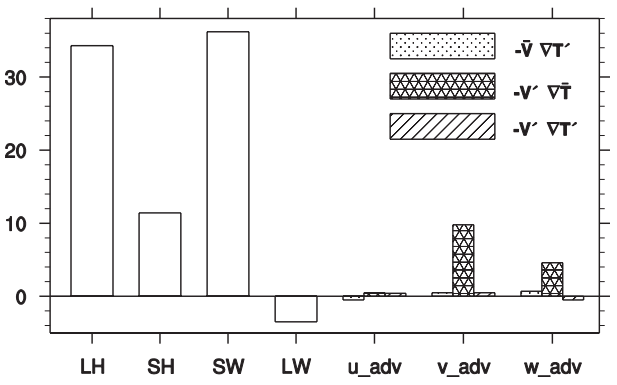

FIG. 6. Contributions of latent heat flux (LH), sensible heat flux (SH), shortwave radiation (SW), and longwave radiation (LW) terms and ocean advection terms (10^{-2} K pentad^{-1}) averaged in the developing phase (from −150° to −30°).

To quantitatively determine the relative importance of the aforementioned processes in causing the SST warming on the intraseasonal time scale, we conduct a mixed layer heat budget analysis. The time series of the observed mixed layer temperature tendency (left-hand side) and the sum of 3D temperature advection and heat flux terms in the KE region is illustrated in Fig. 5a. The gross pattern is quite similar, implying that the residual term is small, although there is a 30° phase lag at the peak warming phase (the lag is primarily attributed to the net surface heat flux term, as one can see in Fig. 5b). The amplitudes of the maximal warming (cooling) tendency during the phases from −150° to −30° (30°–150°) are close to the observed values.

The relative contributions of the ocean advection terms and the surface heat flux terms in the SST tendency are shown in Fig. 5b. The amplitude of the heat flux terms is about five times as large as that of the ocean advection terms.

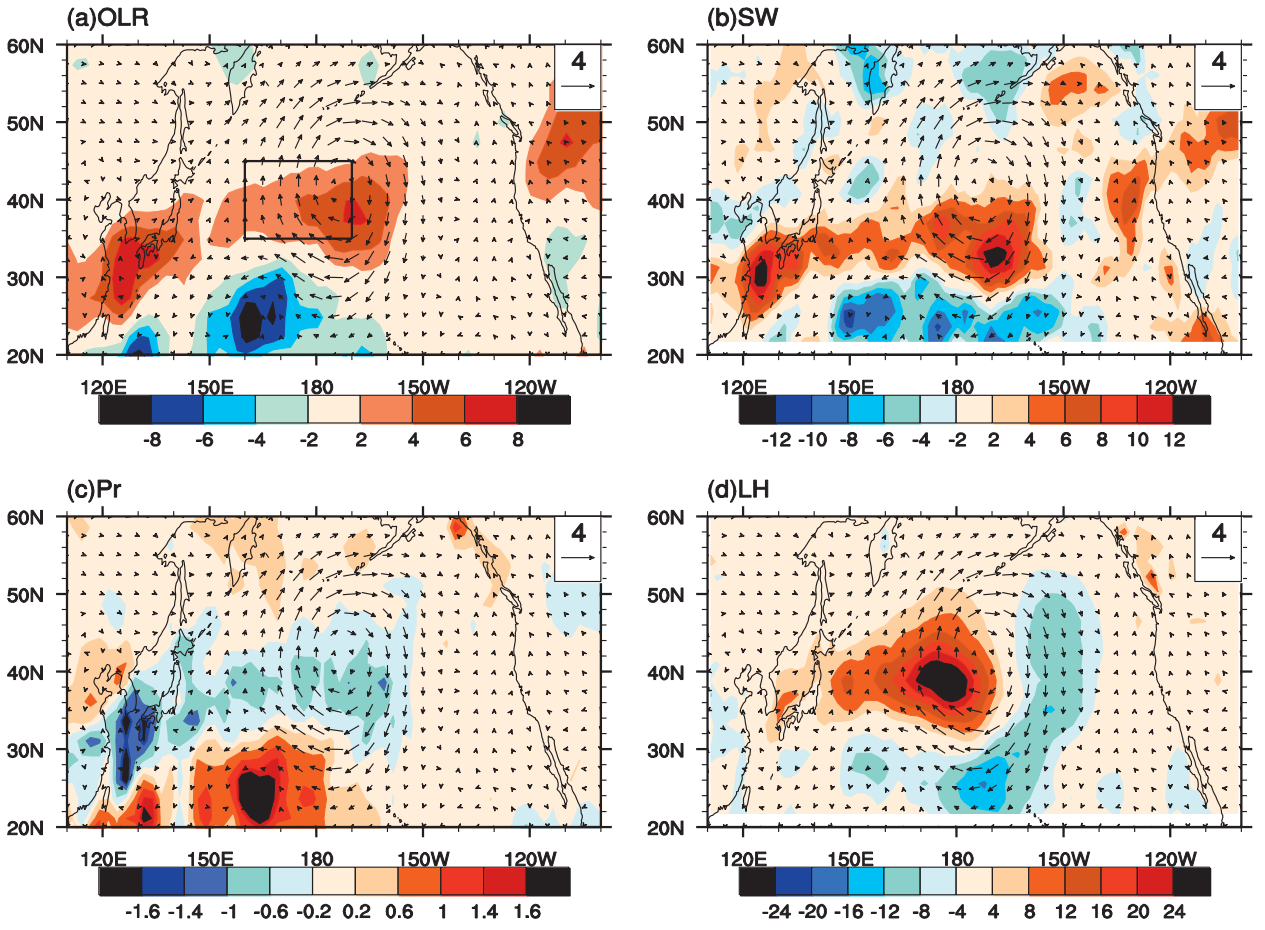

FIG. 7. Composite patterns of (a) OLR anomalies (W m^{-2}) (shaded), (b) surface net SW anomalies (W m^{-2}) (shaded), (c) CMAP precipitation anomalies (Pr) (mm day^{-1}) (shaded), and (d) surface LH anomalies (W m^{-2}) (shaded) averaged in developing phase (−150° to −30°); 1000-hPa wind anomalies are plotted in all panels. In both (b) and (d) a positive heat flux value indicates heating the ocean. The box in (a) represents the maximum intraseasonal SST variability region (35°–45°N, 160°E–170°W).

We further decompose the net surface heat flux into net shortwave radiation, net longwave radiation, latent heat flux, and sensible heat flux components and decompose the 3D ocean temperature advection into the zonal, meridional, and vertical components. For each advection component, it can be further separated into linear (anomalous advection by either the mean temperature gradient or the mean current) and nonlinear (anomalous temperature advection by the anomalous current) advection terms. Figure 6 depicts the relative importance of these terms above during the SST developing phase. It is clear that the net shortwave radiation term and the surface latent heat flux term are the two dominant terms in determining the intraseasonal SST tendency. The sensible heat flux also has a positive contribution but with a much smaller magnitude, while the longwave radiation anomalies tend to offset the other heat flux effect but with a much smaller magnitude. The contributions of the advection terms mainly come from the meridional advection of the mean temperature gradient by anomalous meridional currents and the vertical advection of the mean temperature gradient by the anomalous vertical velocity.

The composite patterns of OLR, precipitation, surface net shortwave radiation, and latent heat flux anomalies averaged during the developing phase are shown in Fig. 7. There are large-scale positive OLR and negative precipitation anomalies over the KE region box. Correspondingly, the surface net shortwave radiation anomalies have a positive value in the region. While the suppressed rainfall is obviously associated with the anomalous anticyclone and pronounced subsidence in the region, the cause of the positive latent heat flux anomaly (i.e., decrease of upward latent heat flux) is unclear.

Examination of the summer mean and anomalous wind patterns (Figs. 8a,b) reveals that in the KE region box the meridional wind anomaly has the same direction as the mean wind. As a result, the wind speed increases (Fig. 8c),

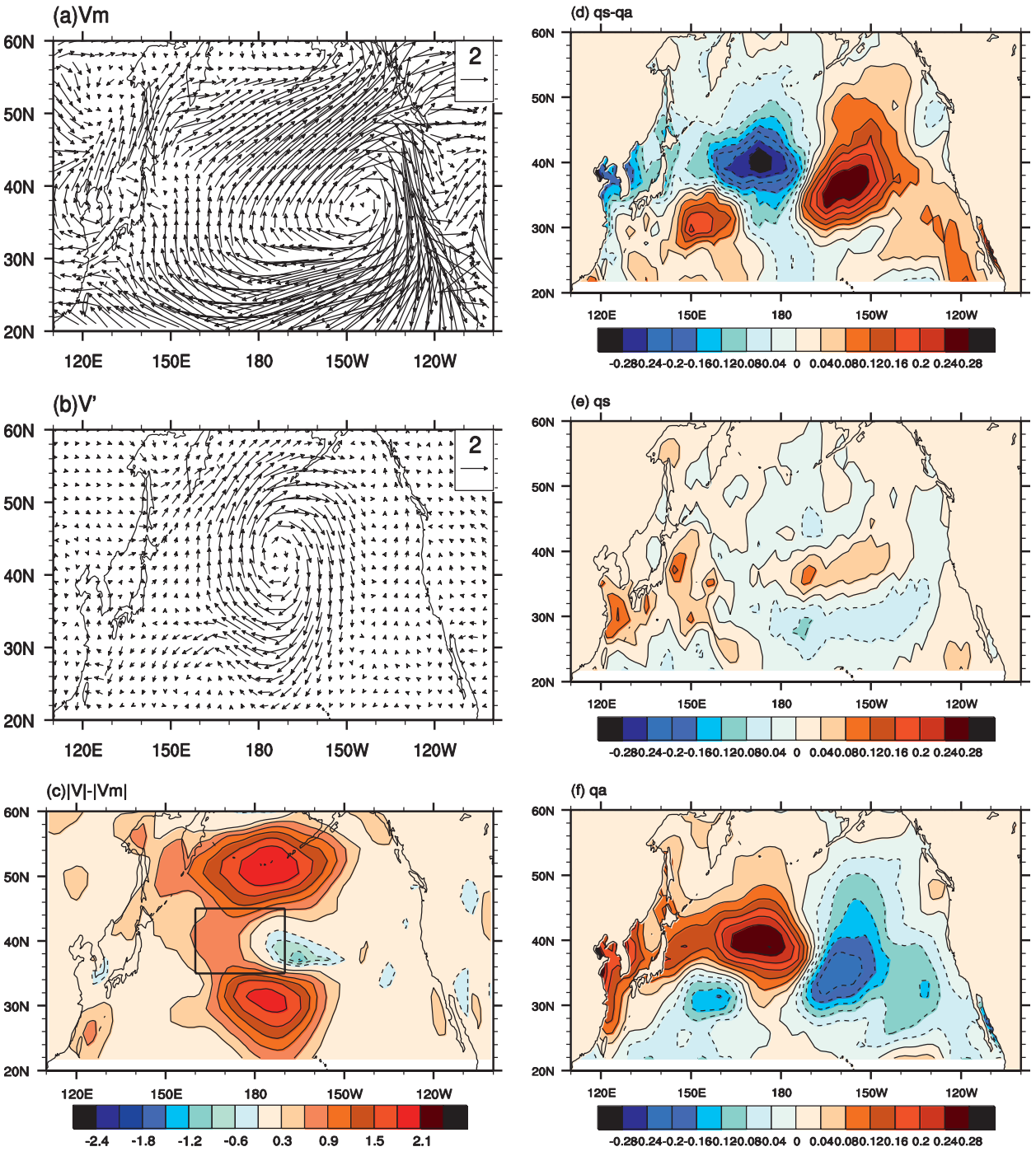

FIG. 8. (a) Boreal summer mean (JJASO) wind at 10 m from NCEP-2 and (b) composite of wind anomalies (m s^{-1}) (vector) at 10 m averaged in developing phase (−150° to −30°). (c) As in (b) but for wind speed anomalies (shaded) at 10 m, and (d) as in (b) but for sea–air specific humidity difference anomalies (g kg^{-1}) (i.e., $q_s - q_a$, where q_s represents the specific humidity anomalies of ocean surface and q_a represents the specific humidity anomalies of near-surface air) (shaded). (e),(f) As in (d) but for q_s and q_a. The key intraseasonal SST warming region (35°–45°N, 160°E–170°W) is marked by the rectangle in (c).

and the primary contributor to the decrease of upward latent heat flux is the negative sea − air specific humidity anomaly difference (i.e., $q_s - q_a$, where q_s represents the specific humidity anomalies of the ocean surface and q_a represents the specific humidity anomalies of near-surface air) (Fig. 8d). A further examination of q_s and q_a shows that the humidity difference is mainly attributed to q_a, which has a much larger positive value compared to q_s

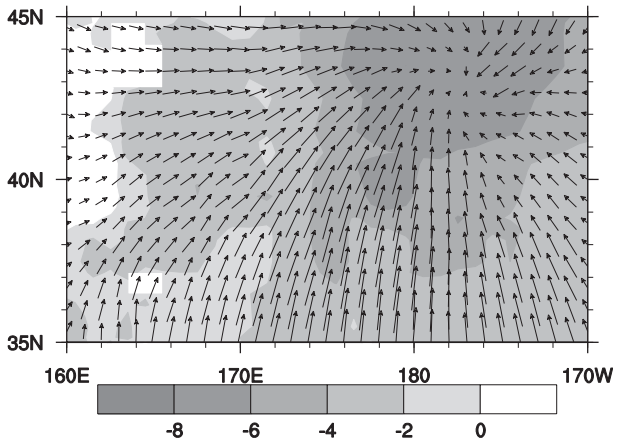

FIG. 9. Composite of the horizontal ocean current (cm s^{-1}) (vectors, z = 10 m) and vertical current (10^{-5} cm s^{-1}) (shaded) anomalies averaged in the upper 50 m during developing phase (−150° to −30°).

(Figs. 8e,f). The positive q_a is due to the positive humidity advection by the northward wind anomalies (figure not shown).

Figure 9 shows the composite patterns of the 20–100-day mixed layer ocean currents and vertical velocity at the base of the mixed layer, averaged during the developing phase. There are clear northward mixed layer currents and downward motion in the KE region. The northward current in response to the surface wind forcing warms the SST through anomalous warm advection from the south. The anomalous downward motion resulting from the anomalous anticyclone wind forcing also contributes partly to the SST warming. During the SSTA decaying phase (say, from phase 60° to 150°), the southward mixed layer currents take place, in association with anomalous upwelling in the upper ocean (figure not shown). The evolution of the anomalous ocean circulations is generally in good agreement with that of the anomalous surface wind field, indicating that they are primarily driven by Ekman process-related wind stress forcing.

5. Ocean feedback to the atmosphere

The above analysis indicates that the intraseasonal SST warming primarily results from the local atmospheric forcing. Does the SST also play an active role to feed back to the atmospheric circulation? To address this question, we examine the detailed structure and evolution characteristics of several key atmospheric variables.

The first variable that we examined is the convective instability parameter, which measures the extent to which the atmosphere is convectively unstable. The convective instability depends on the vertical gradient of atmospheric equivalent potential temperature (θ_{se}). Figure 10a shows the evolution of θ_{se} vertical profiles in the lower troposphere averaged over the KE region (35°–45°N, 160°E–170°W). Note that during the phases from −180° to −30°, the atmosphere is in a convectively stable condition, but this stability decreases as the SST warms. At phase 0°, it is in a neutral condition. From phase 30° on, the atmosphere becomes convectively unstable. Such a feature is consistent with the OLR and rainfall evolutions shown in Fig. 4.

Given the fact that the transition of the atmospheric circulation pattern from an anticyclonic flow to a cyclonic flow just occurs during the phases from 0° to 60° (this period is defined as ''the atmospheric transitional phase'' in the following) when the atmosphere just becomes convectively unstable, it is argued that the atmospheric precipitation and heating anomalies induced by the change of the convective instability are responsible for the anticyclone-to-cyclone transition. What causes the increase of the convective instability parameter from phase 0° to 60°? An examination of time evolution of the vertical θ_{se} difference between 1000 and 850 hPa (Fig. 10b) reveals that the convective instability parameter continues to increase from phase 0° to phase 60°, which helps to trigger the anomalous convection in the region (Fig. 4). Since the change of the convective instability parameter depends on the relative changes of air temperature and specific humidity at both levels, it is necessary to examine their relative contributions.

One way to assess the relative importance of ΔT and Δq (Δ represents the difference between 1000 and 850 hPa) in causing $\Delta\theta_{se}$ changes from phase 0° to 60° is to keep one variable (either ΔT or Δq) unchanged (i.e., keep the same value at phase 0°) while letting the other variable vary. Figure 11 shows the calculation results. Obviously, during the transitional phase the ΔT change is crucial, while the Δq change is negligible. Thus, the strengthened convective instability parameter from phase 0° to 60° is primarily attributed to the distinctive evolutions of air temperature at the lower (1000 hPa) and upper (850 hPa) levels.

What causes the different temperature tendencies at the upper and lower levels? Figure 12a plots the evolution of air temperature at both 1000-hPa and 850-hPa levels. During the transitional phase, the temperature at both levels decreases with time, but the temperature decreases more rapidly at 850 than at 1000 hPa.

According to Eq. (3), the temperature tendency depends on adiabatic and diabatic terms. We first conduct a budget analysis to reveal the difference of the contributions from the adiabatic terms between the 850-hPa and 1000-hPa levels. Figure 12b shows the sum of all adiabatic temperature tendency terms averaged in the transitional phase. It is noted that the adiabatic cooling tendency is

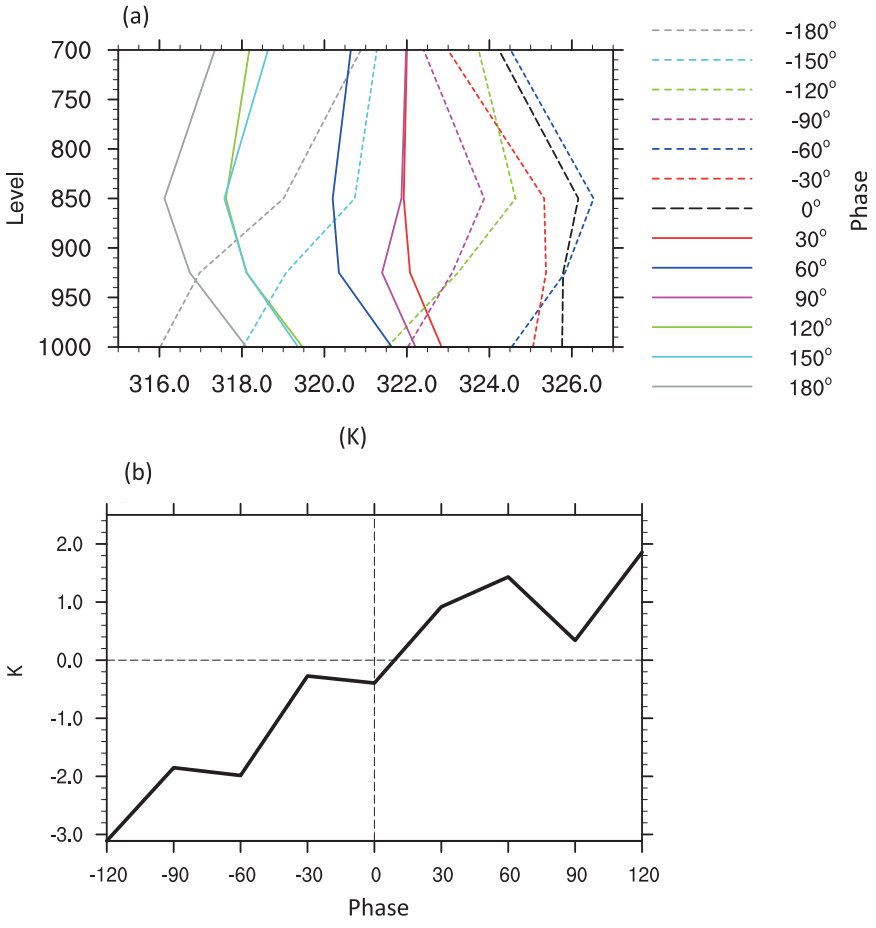

FIG. 10. Phase evolution of (a) vertical profiles of the composite θ_{se} and (b) the convective instability parameter $\Delta\theta_{se}$ (i.e., $\theta_{se\_1000} - \theta_{se\_850}$) averaged in the KE box region (35°–45°N, 160°E–170°W).

greater at 1000 than 850 hPa. This implies that the diabatic heating must play an important role in reducing the adiabatic cooling at the 1000-hPa level. Without the diabatic heating effect, air temperature at 1000 hPa would decrease much faster than that at 850 hPa.

A further diagnosis of apparent heat and moisture sources (Q1 and Q2) indicates that the diabatic heating near the surface is primarily attributed to condensational heating. This implies that surface evaporation plays a role in maintaining near-surface moisture during the transitional phase while air temperature drops at 1000 hPa. Figure 13a shows the composite pattern of the surface latent heat flux averaged in the transitional period. A negative heat flux anomaly (i.e., increase of upward latent heat flux) appears in the KE region. Because the surface latent heat flux anomaly depends on both anomalous wind speed and $(q_s - q_a)$, we further diagnose the relative contributions of the wind speed and q_s/q_a. Over the KE region box, the wind speed decreases (Fig. 13b), which alone would cause the decrease of the upward latent heat flux. Thus, a positive $(q_s - q_a)$ in the region is a sole factor that contributes to the increase of the upward latent heat flux. A further examination reveals that the result of $(q_s - q_a)$ is primarily attributable to q_s (Figs. 13c–e), which is mainly affected by the SSTA. Therefore, the above analysis reveals the important role of the warm SSTA in inducing the convective instability during the transitional phase, leading to the anticyclone-to-cyclone transition in the atmosphere.

Consistent with the change of the atmospheric convective instability parameter and precipitation, the vertical profiles of the diagnosed apparent heat source (Q_1, Fig. 14) show a similar evolution feature. The low-level diabatic heating rate is negative prior to phase 0° and becomes positive after phase 0°. During the atmospheric transitional phase, the maximum heating rate is confined at the bottom level, indicating the SST effect. The second maximum heating rate is near the level of 400 hPa, implying the latent heating released by convective precipitation.

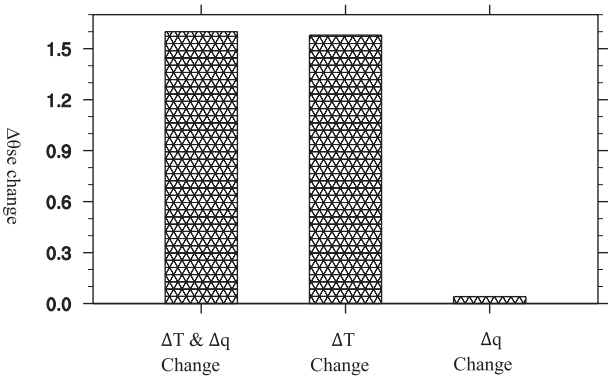

FIG. 11. Relative contributions to the change of $\Delta\theta_{se}$ (i.e., $\theta_{se\_1000} - \theta_{se\_850}$) from phase 0° to 60° by the change of ΔT (i.e., $T_{1000} - T_{850}$) and Δq (i.e., $q_{1000} - q_{850}$).

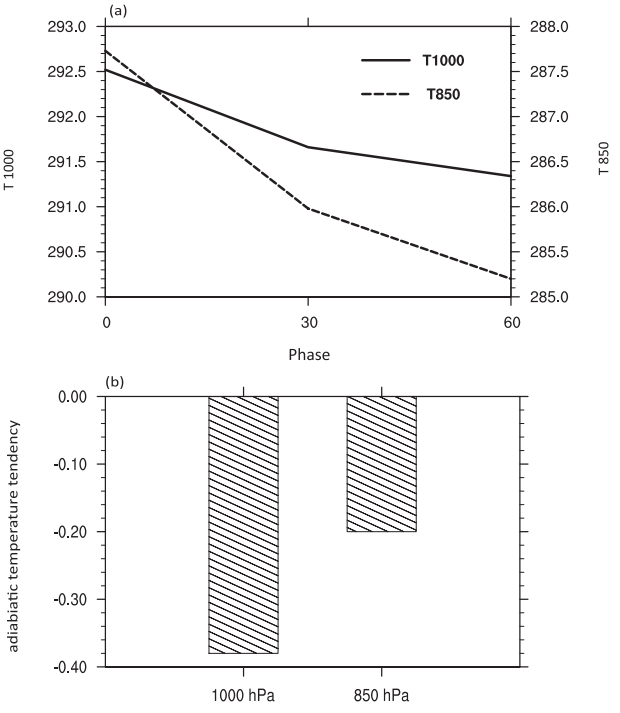

FIG. 12. (a) Composite evolution (from phase 0° to 60°) of air temperature (K) at 1000 hPa (solid line) and 850 hPa (dashed line) and (b) sum of the adiabatic temperature tendency terms ($-u\partial T/\partial x - v\partial T/\partial y - \omega\partial T/\partial p + \alpha\omega/C_p$) (K day^{-1}) averaged in transitional phase (0°–60°) at 1000 and 850 hPa, respectively.

An interesting feature associated with the initial atmospheric response to the heating is a quick baroclinic adjustment. This baroclinic process can be clearly seen in the temporal evolution of the geopotential height anomalies over the KE region (Fig. 15). From phase −150° to −30°, the height fields show positive anomalies with quasi-barotropic vertical structure (with the maximum values confined at the upper troposphere). From phase 0° to 30°, the height anomaly field exhibits a baroclinic structure with the negative anomalies at the lower level and positive anomalies at the upper level. However, the baroclinic process is weak and has a short duration, and the baroclinic structure is quickly replaced by a barotropic vertical profile, which may be attributed to the synoptic eddy feedback in the midlatitudes (e.g., Peng et al. 1995). As a result, the long-time (e.g., monthly, or a half cycle of ISO) averaged height anomalies would appear to have a quasi-barotropic structure. Thus the high-frequency data analysis reveals finescale midlatitude atmospheric evolution features in response to underlying SSTA forcing.

To further verify the heating-induced quick baroclinic process and the baroclinic-to-barotropic transition, an idealized anomaly AGCM experiment was conducted (see the model description in section 2d). Figure 16a shows the horizontal distribution of a specified diabatic heating field. The maximum heating is located over the KE region, with a pattern the same as for the SST anomalies at phase 0° (see Fig. 2). The vertical profile of the heating is displayed in Fig. 16b. It has a maximum in the middle troposphere to mimic the rainfall-induced convective heating. The specified heating is kept constant during the first five days and then gradually reduced to zero (shown in Fig. 16d). The response of the local geopotential height anomaly to the specified heating is shown in Fig. 16c. Note that shortly after a baroclinic response (with a low pressure anomaly at the lower level and a high pressure anomaly at the upper level), the midlatitude atmosphere becomes quasi-barotropic, with low pressure anomalies appearing throughout the troposphere. The numerical experiment confirms the role of atmospheric convective heating in the quick setup of a baroclinic process and the baroclinic-to-barotropic transition.

The observational analysis and modeling results above suggest a two-way interaction between the ocean and atmosphere on the intraseasonal time scale over the KE region. On one hand, SSTAs are caused by the atmospheric forcing (in the presence of a low-level anticyclone perturbation). On the other hand, the SSTAs contribute to the anticyclone-to-cyclone transition through a baroclinic response to the atmospheric heating associated with the change of convective instability. Such a two-way interaction may be further inferred from the lead–lag correlation between the unfiltered SSTA and geopotential height fields in the upper, middle, and lower troposphere (Fig. 17). Significant positive correlations occur from around day −10 to −5 and exceed the 95% confidence level, suggesting that positive height anomalies lead positive SSTA. This indicates an atmospheric driving of the ocean. It is also noted that significant (slightly over a 90% confidence level) negative correlations occur at around day +10, suggesting that positive SSTAs lead negative height

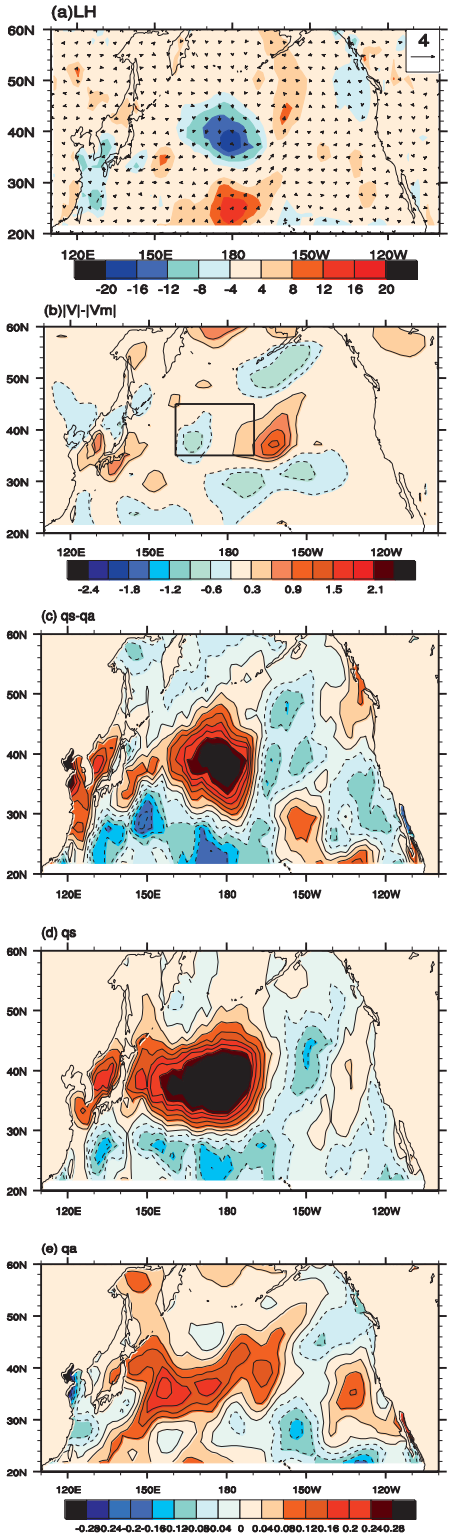

FIG. 13. (a) Composite patterns of surface latent heat flux (LH) anomaly (W m^{-2}) (shaded) and 1000-hPa wind anomaly (m s^{-1}) (vectors) averaged in the transitional phase. A positive heat flux indicates heating the ocean. (b)–(e) As in Figs. 8c–f but for the values averaged in the transitional phase.

anomalies. This indicates an oceanic feedback to the atmosphere. Although raw data were used in the above correlation calculations, the results clearly indicate a half cycle of a coupled air–sea mode with a duration of ~20 days, which is in the intraseasonal periodicity.

6. Summary and discussion

The structure and evolution characteristics of the intraseasonal (20–100 day) SST anomaly and associated circulation patterns over the KE region during boreal summer are investigated based on observed daily SST and rainfall fields, NCEP-2 reanalysis data, and GODAS data. The intraseasonal SST warming is accompanied by an anomalous large-scale anticyclonic cell and suppressed rainfall and convection in the overlying atmosphere. The anomalous atmospheric circulation has an equivalent-barotropic vertical structure. During the SST cooling phase, the atmospheric circulation and rainfall patterns generally display a mirror image opposite to those during the SST warming phase.

The intraseasonal SST variability in the KE region is primarily attributed to the surface heat flux forcing. A mixed layer heat budget analysis reveals that the shortwave radiation and latent heat fluxes are two primary contributors for SST warming. The surface sensible heat flux and oceanic horizontal and vertical advection also play a role, but with a much smaller magnitude. Anomalous meridional Ekman currents advect heat from the south. Meanwhile, anomalous downwelling induced by the anticyclonic wind forcing also contributes to the surface warming by reducing the mean upwelling/vertical mixing.

The SST warming due to the atmospheric forcing may exert a feedback to the atmosphere through triggering the atmospheric convective instability. It is noted that the upward surface latent heat flux induced by the warm SSTA at the transitional phase modulates the near-surface moisture, condensational heating, and air temperature tendency in such a way that the lower troposphere becomes convectively unstable. The convective instability induces anomalous precipitation and convective heating, leading to the transition of low-level atmospheric circulation from an anomalous anticyclone to an anomalous cyclone.

The increase of the convective instability parameter in the earlier development stage (from phase −120° to −30°; Fig. 10b) is primarily caused by a higher increasing rate of θ_{se} at 1000 hPa than at 850 hPa (Fig. 10a). The faster increase of θ_{se} in the lower level is attributed to the greater increases of both air temperature and specific humidity at 1000 hPa in association with the SST warming. However, during that time the atmosphere is convectively

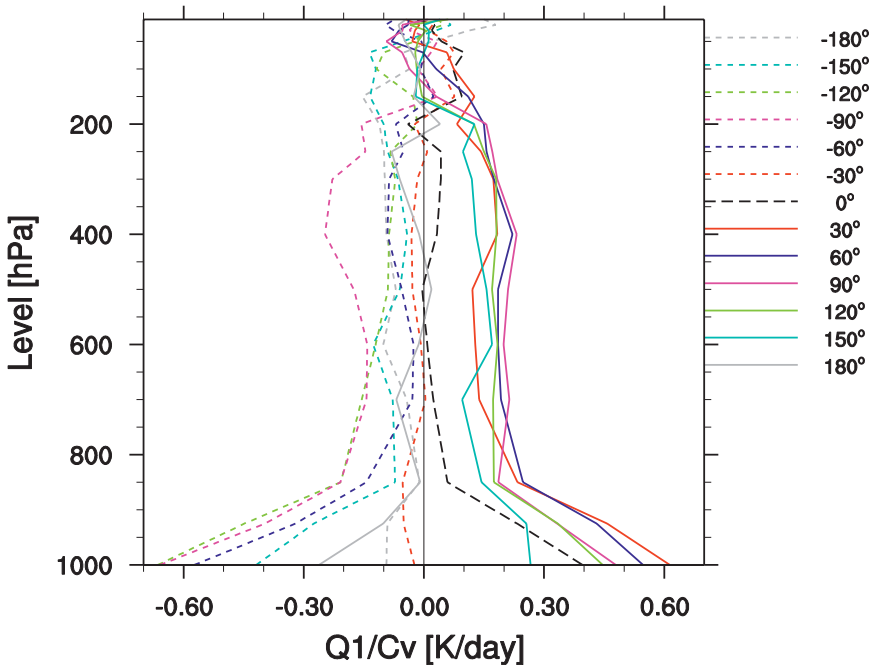

FIG. 14. Phase evolution of the apparent heat source (Q_1) averaged in the KE box region (35°–45°N, 160°E–170°W).

stable. As a result, the SST warming during this period does not affect the atmospheric heating and circulation, and the SSTA in this period are primarily a passive response to the atmosphere. Only after the convective instability is triggered do the SSTAs have an active role in affecting the overlying atmospheric circulation. The initial atmospheric response to the atmospheric heating is a quick setup of a baroclinic vertical structure in the height field. However, because of the strong eddy feedback in midlatitudes, this baroclinic structure is quickly replaced by a barotropic vertical structure.

An anomaly AGCM experiment with specified summer mean flow and midlatitude heating anomaly further confirms such a baroclinic-to-barotropic transition process. Both observational and modeling studies above suggest a negative SST feedback during the atmospheric transitional phase, which is helpful for the transition of the atmospheric ISO in the midlatitudes. This negative SST feedback is quite different from a positive feedback between the barotropic atmosphere and the underlying ocean in the extratropics as derived from monthly mean anomaly fields (e.g., Kushnir et al. 2002). Keep in mind that in most of the ISO phases shown in Fig. 15, the atmosphere is barotropic. As a result, the long-time average of the atmospheric response displays a barotropic structure, consistent with the previous result.

Previous studies demonstrated that significant intraseasonal oscillations exist in the atmospheric circulations over the midlatitude North Pacific in boreal summer (e.g., Kawamura et al. 1996). However, the origin of this midlatitude ISO remains unclear. One possible origin is tropical ISO forcing (e.g., Kawamura et al. 1996; Pan and Li 2008). A composite analysis with a bigger domain shows that the SSTA in the KE region are, indeed, somehow related to OLR and wind anomalies near the Philippine Sea, at least at phases 0° and 30° (figure not shown). This indicates a possible connection with the western North Pacific (WNP) circulation and heat source, consistent with previous studies (e.g., Kawamura et al.

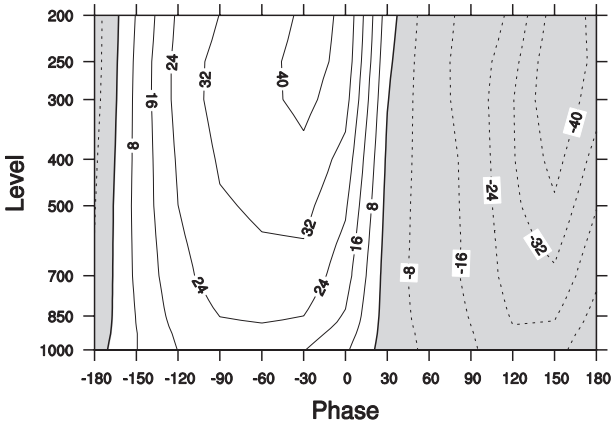

FIG. 15. Temporal evolution of the geopotential height anomalies (m) averaged in the KE region (35°–45°N, 160°E–170°W).

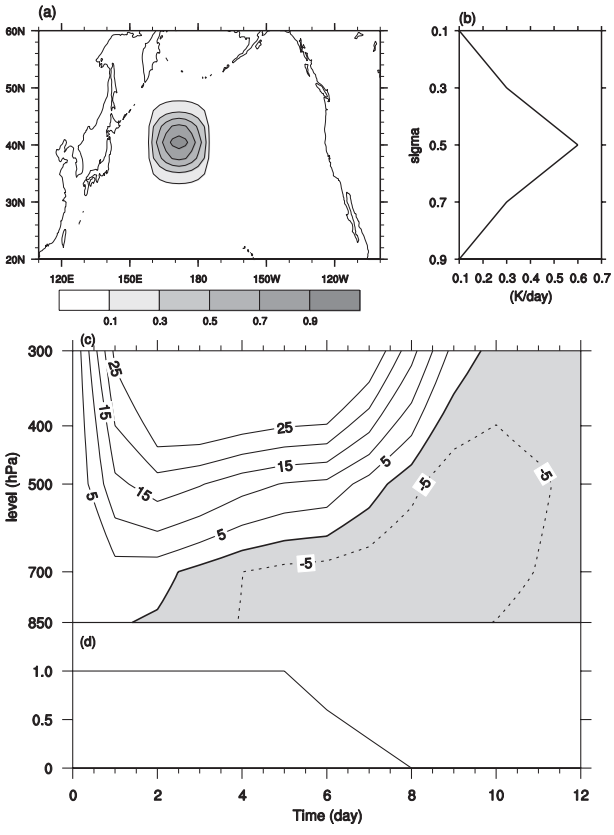

FIG. 16. (a) Horizontal distribution and (b) vertical profile of the initial diabatic heating (K day^{-1}) prescribed in the AGCM. The vertical coordinate in (b) represents sigma levels in the model. (c) Hovmöller diagram of the geopotential height anomalies (m) averaged in the KE box region (35°–45°N, 160°E–170°W) derived from the numerical experiment. The bold contour represents the zero line. (d) The evolution of the heating rate (K day^{-1}) prescribed in the AGCM.

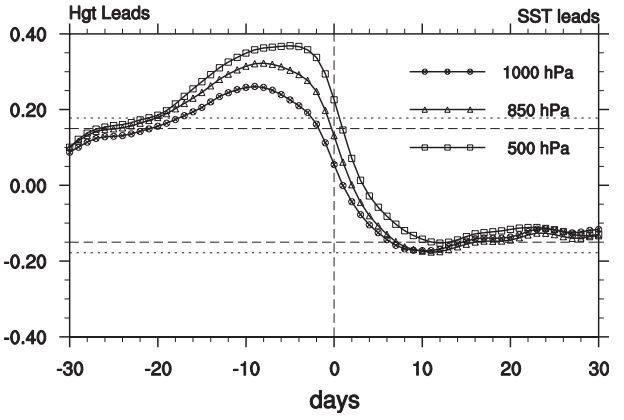

FIG. 17. Lead–lag correlation coefficients between the unfiltered geopotential height anomalies at 1000 hPa (circles), 850 hPa (triangles), and 500 hPa (squares) and SSTA in the KE box region (35°–45°N, 160°E–170°W). The dashed (dotted) lines represent a 90% (95%) significance level.

1996), that suggested the Madden–Julian oscillation convection in the WNP can influence the midlatitude ISO through Rossby wave dispersion. The two-way interaction scenario described in this study suggests that the origin of the atmospheric intraseasonal oscillation over the KE region may arise partially from the local ocean–atmosphere interaction. Thus, in addition to the tropical forcing we propose another possible mechanism; that is, the combined effect of local atmospheric baroclinic instability and air–sea interaction may favor the development of perturbations on the intraseasonal time scale. While classical baroclinic instability theories showed that the midlatitude atmosphere prefers the most unstable mode at a synoptic scale (with a period of a week or so) in the absence of the ocean coupling (e.g., Holton 2004), it is likely that, with the coupling of the ocean, the preferred time scale of the most unstable mode might shift or extend to the intraseasonal band. This hypothesis, however, needs to be approved or disproved in a coupled theoretical framework. A related question is what percentage of the atmospheric ISO in the midlatitude North Pacific is caused by local processes versus remote forcing from the tropics. To address this issue, idealized numerical model experiments with isolated tropical forcing have been conducted. We are currently diagnosing such model experiments, and results will be reported elsewhere.

Acknowledgments. This work was supported by the National Basic Research Program of China (2010CB951904). TL was supported by NSF Grant AGS-1106536 and NOAA Grant N000140810256 and by the International Pacific Research Center that is sponsored by the Japan Agency for Marine-Earth Science and Technology (JAMSTEC), NASA (NNX07AG53G), and NOAA (NA17RJ1230).

REFERENCES

Alexander, M., 1992: Midlatitude atmosphere–ocean interaction during El Niño. Part I: The North Pacific Ocean. *J. Climate,* **5,** 944–958.

——, I. Blade, M. Newman, J. R. Lanzante, N.-C. Lau, and J. D. Scott, 2002: The atmospheric bridge: The influence of ENSO teleconnections on air–sea interaction over the global oceans. *J. Climate,* **15,** 2205–2231.

Behringer, D., and Y. Xue, 2004: Evaluation of the global ocean data assimilation system at NCEP: The Pacific Ocean. Preprints, *Eighth Symp. on Integrated Observing and Assimilation Systems for Atmosphere, Oceans, and Land Surface,* Seattle, WA, Amer. Meteor. Soc., 2.3. [Available online at http://ams.confex.com/ams/pdfpapers/70720.pdf.]

Cayan, D. R., 1992: Latent and sensible heat flux anomalies over the northern Oceans: Driving the sea surface temperature. *J. Phys. Oceanogr.,* **22,** 859–881.

Czaja, A., and C. Frankignoul, 1999: Influence of the North Atlantic SST on the atmospheric circulation. *Geophys. Res. Lett.,* **26,** 2969–2972.

——, and ——, 2002: Observed impact of Atlantic SST anomalies on the North Atlantic Oscillation. *J. Climate,* **15,** 606–623.

Duchon, C., 1979: Lanczos filtering in one and two dimensions. *J. Appl. Meteor.,* **18,** 1016–1022.

Frankignoul, C., 1985: Sea surface temperature anomalies, planetary waves, and air-sea feedback in the middle latitudes. *Rev. Geophys.,* **23,** 357–390.

——, and K. Hasselmann, 1977: Stochastic climate models, Part II Application to sea-surface temperature anomalies and thermocline variability. *Tellus,* **29,** 289–305.

——, and R. Reynolds, 1983: Testing a dynamical model for midlatitude sea surface temperature anomalies. *J. Phys. Oceanogr.,* **13,** 1131–1145.

Held, I. M., and M. J. Suarez, 1994: A proposal for the intercomparison of the dynamical cores of atmospheric general circulation models. *Bull. Amer. Meteor. Soc.,* **75,** 1825–1830.

——, S. W. Lyons, and S. Nigam, 1989: Transients and the extratropical response to El Niño. *J. Atmos. Sci.,* **46,** 163–174.

Hendon, H. H., and D. L. Hartmann, 1982: Stationary waves on a sphere: Sensitivity to thermal feedback. *J. Atmos. Sci.,* **39,** 1906–1920.

Holton, J. R., 2004: *Introduction to Dynamic Meteorology*. Academic Press, 535 pp.

Jiang, X.-A., and T. Li, 2005: Reinitiation of the boreal summer intraseasonal oscillation in the tropical Indian Ocean. *J. Climate,* **18,** 3777–3795.

Kanamitsu, M., W. Ebisuzaki, J. Woollen, S.-K. Yang, J. J. Hnilo, M. Fiorino, and G. L. Potter, 2002: NCEP–DOE AMIP-II Reanalysis (R-2). *Bull. Amer. Meteor. Soc.,* **83,** 1631–1643.

Kawamura, R., 1994: A rotated EOF analysis of global sea surface temperature variability with interannual and interdecadal scales. *J. Phys. Oceanogr.,* **24,** 707–715.

——, T. Murakami, and B. Wang, 1996: Tropical and mid-latitude 45-day perturbations over the western Pacific during the northern summer. *J. Meteor. Soc. Japan,* **74,** 867–890.

Kushnir, Y., W. A. Robinson, I. Bladé, N. M. J. Hall, S. Peng, and R. Sutton, 2002: Atmospheric GCM response to extratropical SST anomalies: Synthesis and evaluation. *J. Climate,* **15,** 2233–2256.

Latif, M., and T. P. Barnett, 1994: Causes of decadal climate variability over the North Pacific and North America. *Science,* **266,** 634–637.

Lau, K.-M., J.-Y. Lee, K.-M. Kim, and I.-S. Kang, 2004: The North Pacific as a regulator of summertime climate over Eurasia and North America. *J. Climate,* **17,** 819–833.

Lau, N.-C., and M. J. Nath, 1996: The role of the ''atmospheric bridge'' in linking tropical Pacific ENSO events to extratropical SST anomalies. *J. Climate,* **9,** 2036–2057.

Li, T., 2006: Origin of the summertime synoptic-scale wave train in the western North Pacific. *J. Atmos. Sci.,* **63,** 1093–1102.

——, Y. Zhang, E. Lu, and D. Wang, 2002: Relative role of dynamic and thermodynamic processes in the development of the Indian Ocean dipole: An OGCM diagnosis. *Geophys. Res. Lett.,* **29,** 2110, doi:10.1029/2002GL015789.

Liebmann, B., and C. A. Smith, 1996: Description of a complete (interpolated) outgoing longwave radiation dataset. *Bull. Amer. Meteor. Soc.,* **77,** 1275–1277.

Namias, J., 1959: Recent seasonal interaction between North Pacific waters and the overlying atmospheric circulation. *J. Geophys. Res.,* **64,** 631–646.

——, 1965: Short-period climatic fluctuations: The nature and cause of climatic abnormalities lasting from a month to a few years are discussed. *Science,* **147,** 696–706.

Pan, L.-L., and T. Li, 2008: Interactions between the tropical ISO and midlatitude low-frequency flow. *Climate Dyn.,* **31,** 375–388.

Park, C.-K., and S. D. Schubert, 1997: On the nature of the 1994 East Asian summer drought. *J. Climate,* **10,** 1056–1070.

Peng, S., L. A. Mysak, J. Derome, H. Ritchie, and B. Dugas, 1995: The differences between early and midwinter atmospheric responses to sea surface temperature anomalies in the northwest Atlantic. *J. Climate,* **8,** 137–157.

Qiu, B., 2003: Kuroshio Extension variability and forcing of the Pacific decadal oscillations: Responses and potential feedback. *J. Phys. Oceanogr.,* **33,** 2465–2482.

Reynolds, R., N. Rayner, T. M. Smith, D. C. Stokes, and W. Wang, 2002: An improved in situ and satellite SST analysis for climate. *J. Climate,* **15,** 1609–1625.

Rodwell, M., and C. Folland, 2002: Atlantic air-sea interaction and seasonal predictability. *Quart. J. Roy. Meteor. Soc.,* **128,** 1413–1443.

Sun, J. Q., W. Yuan, and Y. Gao, 2008: Arabian Peninsula-North Pacific Oscillation and its association with the Asian summer monsoon. *Sci. China, Ser. D: Earth Sci.,* **51,** 1001–1012.

Tomita, T., S.-P. Xie, and M. Nonaka, 2002: Estimates of surface and subsurface forcing for decadal sea surface temperature variability in the mid-latitude North Pacific. *J. Meteor. Soc. Japan,* **80,** 1289–1300.

Wang, B., R. Wu, and T. Li, 2003: Atmosphere–warm ocean interaction and its impacts on Asian–Australian monsoon variation. *J. Climate,* **16,** 1195–1211.

Wang, W., and M. J. McPhaden, 1999: The surface layer heat balance in the equatorial Pacific Ocean. Part I: Mean seasonal cycle. *J. Phys. Oceanogr.,* **29,** 1812–1831.

Xie, P., and P. Arkin, 1997: Global precipitation: A 17-year monthly analysis based on gauge observations, satellite estimates, and numerical model outputs. *Bull. Amer. Meteor. Soc.,* **78,** 2539–2558.

Zhu, Q. G., Y. Teng, and G. Xu, 2000: The possible mechanism of the effects of SSTA in North Pacific on east China summer rainfall (in Chinese). *Nanjing Inst. Meteor.,* **23,** 1–8.